JGR Solid Earth

RESEARCH ARTICLE
10.1029/2018JB017100

**Key Points:**
- The large pores in the examined unconsolidated sandstone dominated the total porosity, and porosity slightly increased after live-brine flooding
- The pore structure of the examined unconsolidated sandstone changed significantly, caused by fines migration during live-brine injection
- The examined sample's permeability drastically decreased due to reattached fines that blocked the pore throats

**Supporting Information:**
- Supporting Information S1

**Correspondence to:**
H. Yu,
yuhy@nwu.edu.cn;
yu.hongyan@curtin.edu.au

**Citation:**
Yu, H., Zhang, Y., Ma, Y., Lebedev, M., Ahmed, S., Li, X., et al. (2019). $CO_2$-saturated brine injection into unconsolidated sandstone: Implications for carbon geosequestration. *Journal of Geophysical Research: Solid Earth*, *124*, 10,823–10,838. https://doi.org/10.1029/2018JB017100

Received 29 NOV 2018
Accepted 16 SEP 2019
Accepted article online 16 OCT 2019
Published online 5 NOV 2019



# $CO_2$-Saturated Brine Injection Into Unconsolidated Sandstone: Implications for Carbon Geosequestration

**Hongyan Yu[1,2,3], Yihuai Zhang[4], Yao Ma[5], Maxim Lebedev[2], Shakil Ahmed[6], Xiaolong Li[1], Michael Verrall[7], Andrew Squelch[2,8], and Stefan Iglauer[9]**

[1]State Key Laboratory of Continental Dynamics and National and Local Joint Engineering Research Center for Carbon Capture Utilization and Sequestration, Department of Geology, Northwest University, Xi'an, China, [2]WA School of Mines: Minerals, Energy and Chemical Engineering, Curtin University, Kensington, Australia, [3]Research Institute of BGP, CNPC, China, [4]The Lyell Centre for Earth and Marine Science and Technology, Heriot-Watt University, Edinburgh, Scotland, United Kingdom, [5]Key Laboratory of Shaanxi Province for Oil and Gas Accumulation Geology, School of Earth Sciences and Engineering, Xi'an Shiyou University, Xi'an, China, [6]CSIRO Energy Business Unit, Australia, [7]Earth Sciences and Resource Engineering, CSIRO, Kensington, Australia, [8]Computational Image Analysis Group, Curtin Institute for Computation, Curtin University, Australia, [9]School of Engineering, Edith Cowan University, Australia

**Abstract** Carbon dioxide ($CO_2$) injection into deep depleted hydrocarbon reservoirs or saline aquifers is currently considered the best approach to large-scale $CO_2$ storage. Importantly, the pore structure and permeability of the storage rock are affected by fines release, migration, and reattachment in the initial stage of $CO_2$ injection, especially in unconsolidated sandstone reservoirs. It is thus necessary to better understand the pore structure changes and the associated permeability evolution during and after $CO_2$ injection. We thus imaged an unconsolidated sandstone at reservoir conditions before and after $CO_2$-saturated brine ("live brine") injection in situ via X-ray microcomputed tomography to explore the effects of fines migration and mineral dissolution induced by $CO_2$ injection. We found that in the examined sample, large pores dominated the total porosity, and porosity slightly increased after live-brine flooding. Moreover, and importantly, the pore structure changed significantly: large pores were further enlarged while small pores shrank or even disappeared. These structural changes in the tested sample were caused by mobilized fines due to the high-fluid interstitial velocity, which eventually reattached to the grains further downstream. Furthermore, the impact of the pore structural changes on permeability were analyzed in detail numerically. These permeability results are consistent with a fines migration mechanism where reattached fines block pore throats and thus decrease permeability drastically. We therefore can conclude that live brine injected into the examined unconsolidated sandstone will slightly improve storage space (porosity slightly increased); however, injectivity may be severely impaired by the permeability reduction.

## 1. Introduction

Carbon dioxide ($CO_2$) injection into deep saline aquifers is currently considered the best solution for reducing $CO_2$ emissions into the atmosphere and to thus mitigate climate change (Bachu, 2015; Iglauer et al., 2016; Nordbotten et al., 2005). It is well established that fine particles present in the sandstone can be released and mobilized (Alvarez et al., 2006; Bedrikovetsky et al., 2012; Civan, 2010; Gruesbeck & Collins, 1982; Lemon et al., 2011; Qajar et al., 2012; Abbasi et al., 2011); fine particles are usually located on the surface of rock grain. Such fines can also subsequently reattach onto other particles (Bertos et al., 2004; Wigand et al., 2008). The stability of fine particles is determined by electrostatic, gravitational, drag, adhesion, and lifting forces (Civan, 2007, 2010; Khilar & Fogler, 1998; Schembre & Kovscek, 2005; Takahashi & Kovscek, 2010; Valdya & Fogler, 1992). The function of electrostatic, gravitational, and adhesion is to attach the fine particles to the rock surface while the drag and lifting forces would detach it. The migration of the fine particles is determined by the attaching force and detaching force. The detached force is determined by flow velocity (Zeinijahromi et al., 2012) and pH (Khilar & Fogler, 1998). The injected $CO_2$ partially reacts to carbonic acid and thus creates an acidic environment (Pentland et al., 2011). The acid naturally reacts with various minerals in the rock, for example, albite, K-feldspar, and glauconite (Ketzer et al., 2009; Lebedev, Zhang, Sarmadivaleh, et al., 2017; Mangane et al., 2013) when exposed to live brine more than 3 hr

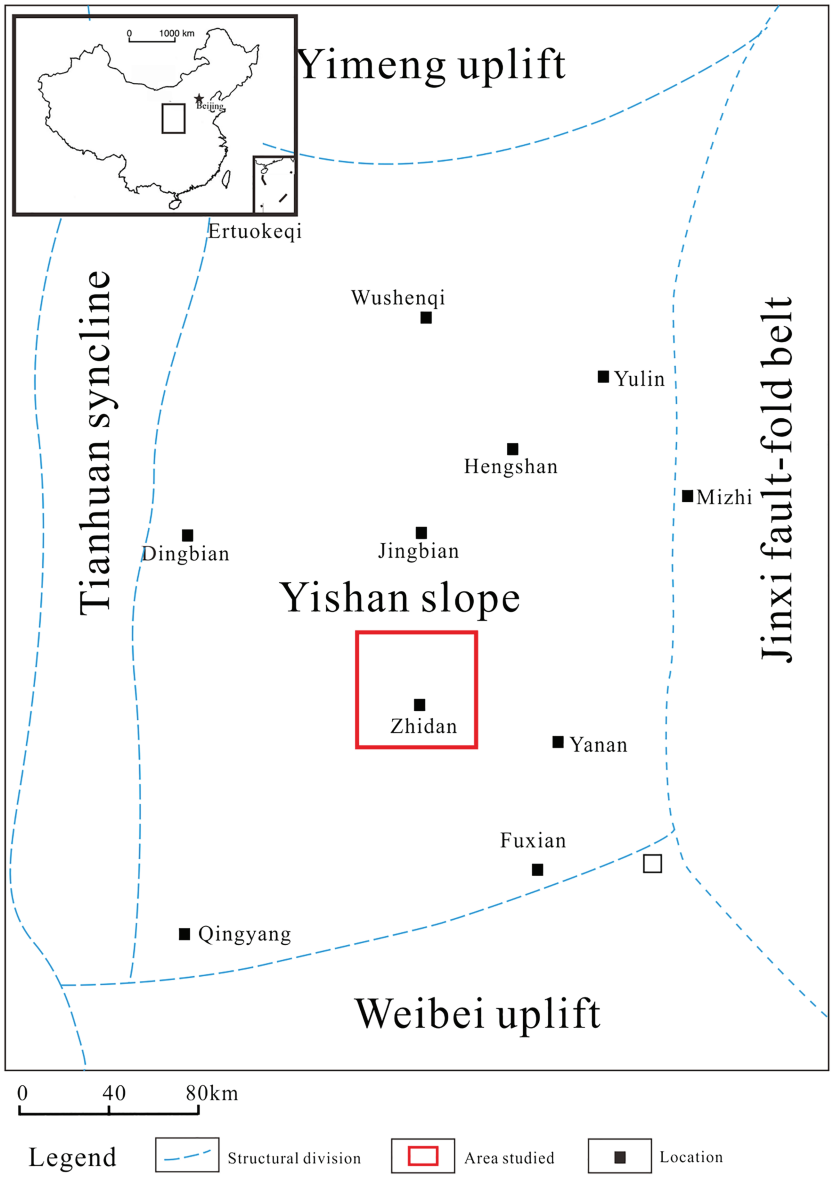


**Figure 1.** Map identifying the origin of the sample.

(Baker et al., 1993; Yasuda et al., 2013). Fines migration and solid reprecipitation change the pore size distribution and pore connectivity, which again significantly influence reservoir-scale fluid dynamics (Al-Khdheeawi et al., 2017, 2018; Hangx et al., 2015), dramatically affect permeability (Al-Yaseri et al., 2015, 2016, 2017; Liu et al., 2018; Reynolds et al., 2014), and storage capacity (Iglauer et al., 2016; Iglauer

**Table 1**
*The stratigraphy of the Gaoqiao area in the Ordos basin.*

| Erathem | System | Formation | Member | Thickness (m) | Sedimentary Facies |
|---|---|---|---|---|---|
| Upper Palaeozoic | Permian | Upper Shihezi | He 1-4 | 90-120 | Shallow lacustrine |
| | | Lower Shihezi | He 5-8 | 120-150 | Fluvial and delta |
| | | Shanxi | Shan 1-2 | 90-110 | Fluvial, delta and swamp |
| | Carboniferous | Taiyuan | Tai 1-2 | 30-70 | Restricted platform |
| | | Benxi | Ben 1-3 | 0-15 | Restricted platform |

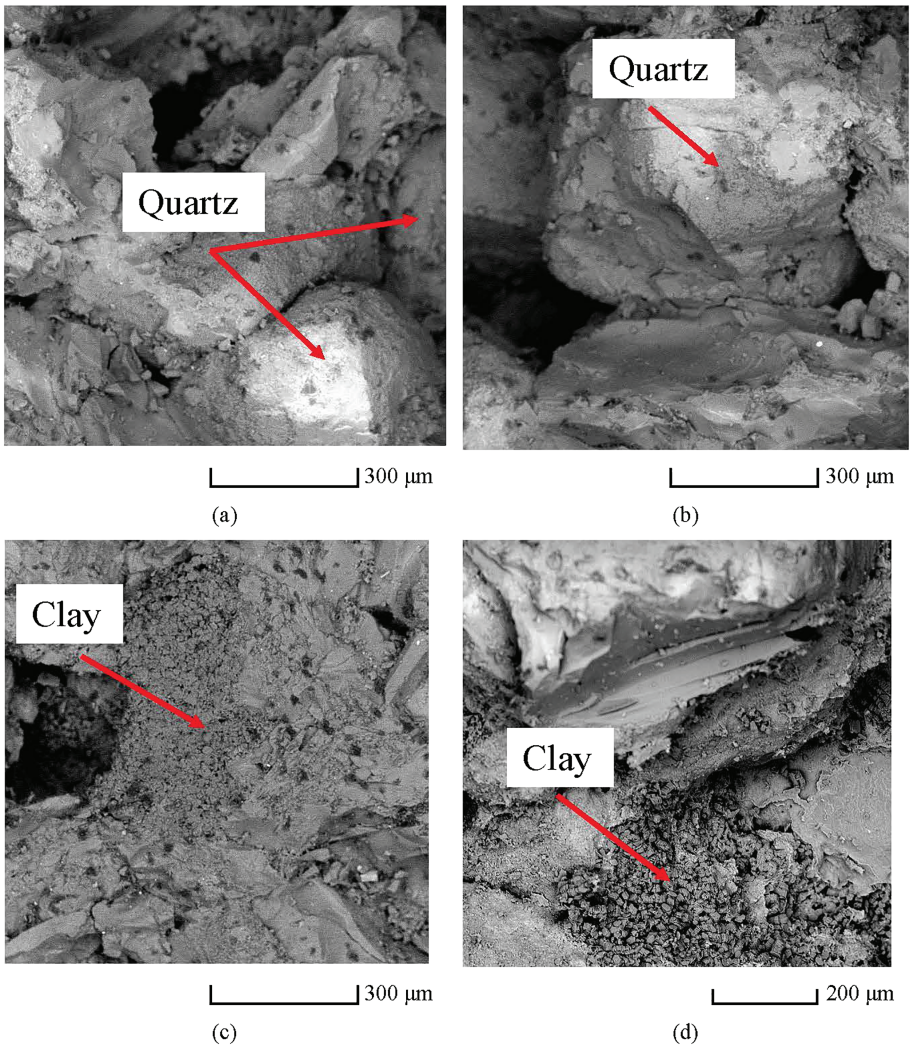


**Figure 2.** SEM images of unconsolidated sandstone sample; (a) and (b) show quartz grains, (c) and (d) show kaolinite clay.

& Lebedev, 2017). This porosity and permeability modification thus pose a significant risk, particularly when permeability is decreased dramatically (formation damage), and as a consequence, $CO_2$ injectivity may be very poor (Iglauer et al., 2014; Lamy-Chappuis et al., 2014; Mangane et al., 2013). These details thus need to be understood in detail to derisk $CO_2$ geostorage projects. In this context, several studies reported $CO_2$ injection into underground sandstone reservoirs (Kampman et al., 2014; Lamy-Chappuis et al., 2014; Pentland et al., 2011; Wigley et al., 2017). These experimental and field studies both demonstrate that significant rock alteration can follow $CO_2$ injection. Kampman et al. (2014) found that Fe–Mg–Ca carbonate minerals dissolved, and the structure of the formation changed drastically after $CO_2$ injection. Thus, calcareous sandstone is rather sensitive to $CO_2$ injection, as porosity and permeability change significantly (Lamy-Chappuis et al., 2014; Sigfusson et al., 2015; Smith et al., 2013).

However, there is a serious lack of understanding in terms of the involved rock-fluid interactions and how fines migration affects the permeability of unconsolidated sandstone reservoirs. Unconsolidated sandstone reservoirs, which are ubiquitous across the world, are some of the main targets for $CO_2$ sequestration (Chen et al., 2017; Pini et al., 2012; Shi et al., 2011); however, the interstitial velocity of the injected fluid and the acid brine formed during $CO_2$ injection can change the pore morphology of the rock (Han et al., 2010; Luhmann et al., 2017; March et al., 2018; Martinez & Hesse, 2016) and thus the rock's permeability. It is thus of critical importance to fully understand the underlying reasons for these changes so that Carbon Geosequestration (CGS) schemes can be optimized. Hence we flooded an unconsolidated

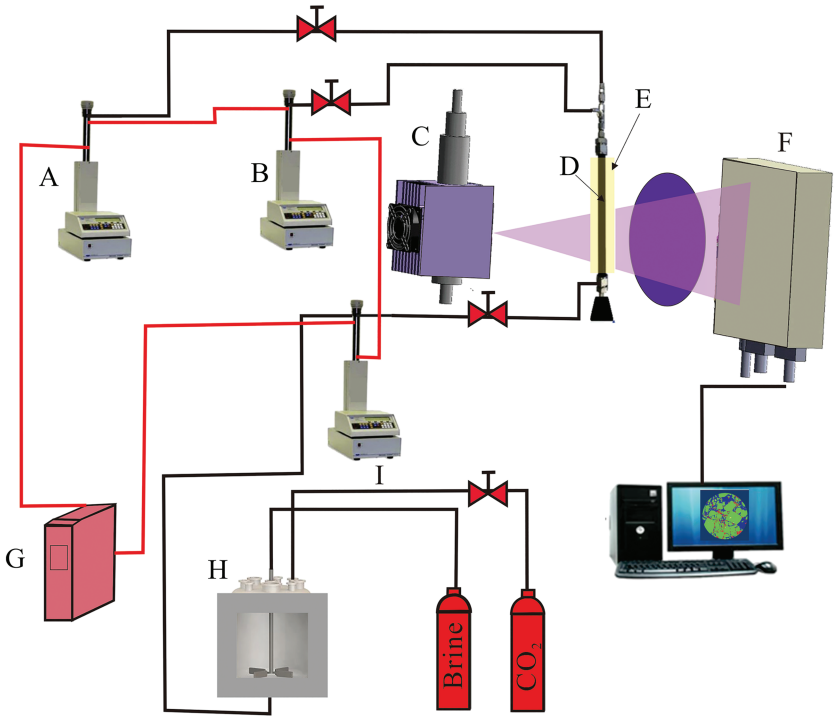


**Figure 3.** Experimental μCT core-flooding apparatus: (A) injection pump, (B) confining pump, (C) x-ray source; (D) core holder, (E) heating tape, (F) detector panel, (G) water bath, (H) reactor, (I) production pump.

sandstone with $CO_2$-saturated brine (live brine) in a laboratory experiment and imaged the microstructural changes directly in situ via high-resolution X-ray microcomputed tomography at reservoir conditions in 3-D. The resulting changes and the underlying mechanisms were examined, and their effects on $CO_2$ geostorage in sandstone are discussed.

## 2. Methodology

### 2.1. Materials

The sample used in this study was acquired from 3,000-m depth of the Ordos Basin (see Figure 1). The Ordos Basin, as the second largest basin in China, is a sedimentary basin formed on the crystalline basement of Precambrian rock with a thick and broadly deposited formation. There are seven first-level tectonic units in this basin, and the sample for this experiment stems from the Gaoqiao area of the Yishan Slope (Figure 1). Specifically, the sandstone in the $He_8$ layer of the Shihezi formation was selected for our study; this formation is one of the most important oil reservoirs in China (Lai et al., 2016; Zhang et al., 2006).

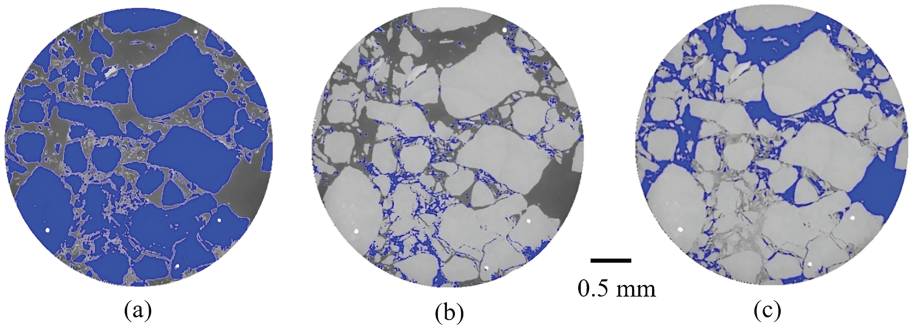


**Figure 4.** Selected 2D slices through the sandstone μCT image: blue = (a) quartz, (b) clays, and (c) pores.

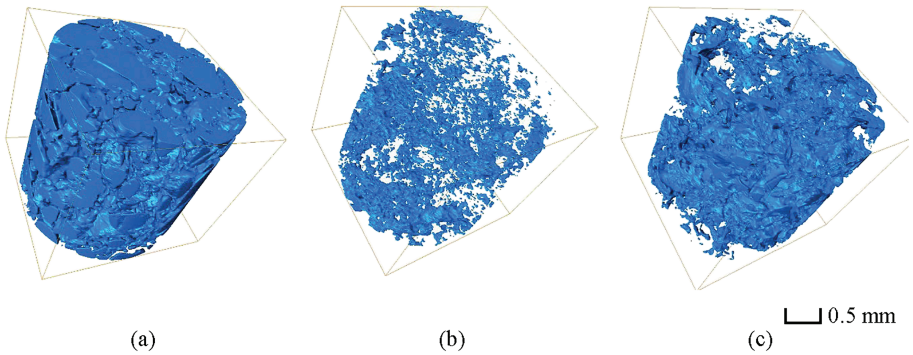


**Figure 5.** 3D visualizations of the different phases identified in the sandstone: blue = (a) quartz, (b) clays, and (c) pores.

Note that the $He_8$ layer of the Shihezi formation (Table 1) is part of the Permian rock in the Gaoqiao area, which was deposited in the braid-river delta plain and braid-river delta front. Previous studies showed that the main component of the $He_8$ sandstone is quartz, followed by metamorphic debris (Ding et al., 2013; Duan et al., 2008; Yang et al., 2005; Zhu et al., 2013). Silicide and calcite formed cementation minerals whereas clay minerals (illite, smectite, and kaolinite) are interstitial minerals. Quartz sandstone dominates the lithology of the $He_8$ layer, showing coarse-grained texture with subangular-subrounded and well-sorted geometry.

A cylindrical subsample (5-mm diameter and 5-mm length) was then drilled from the main plug for the core in this experiment. The sample was composed of quartz (77 wt%), mixed-layer illite/smectite (10 wt%), illite (2 wt%), kaolinite (10 wt%), and chlorite (1 wt%; measured by a Bruker-AXS D9 Advance diffract Meter). The sample was then imaged by scanning electron microscopy and analyzed by energy dispersive spectroscopy (Acquafredda & Paglionico, 2004; Zhang et al., 2016) to study the fine-scale mineral distribution characteristics (Figure 2). Clearly, quartz grains were very large (200–500 μm) and interstitial pores (20–300 μm) between the quartz grains were filled with kaolinite clay. Note that the bulk moduli range from 12–32 GPa while shear moduli range from 12–28 GPa (Ma et al. 2011), which is similar to typical sandstone but slightly lower due to low cementation.

### 2.2. X-ray Microcomputed Tomography In Situ Core Flooding Test

The subplug was then mounted into an X-ray transparent core holder (Iglauer & Lebedev, 2017; Lebedev, Zhang, Mikhaltsevitch, et al., 2017; Zhang et al., 2016), placed in an Xradia Versa 500 XRM X-ray microtomograph (μCT), and connected to a core flooding system. Figure 3 illustrates the setup of the whole apparatus; the following experimental procedure was then applied:

1. The core holder and all tubes were vacuumed for 24 hr to remove all air from the system.
2. All wetted parts of the system (including core holder, injection pump, production pump, and confining pump) were then isothermally heated to 323 K (50 °C) with heating tape and continuously circulating warm water.
3. Initially, the confining pressure was raised to 5 MPa, and the sample was μCT imaged at a high resolution of $(3.43\ \mu m)^3$ in situ in a dry state.
4. Subsequently, $CO_2$-saturated brine (live brine, which was prepared in a separate mixing reactor; compare the procedure described by El-Maghraby et al., 2012) was injected into the sample at a constant flow rate (0.1 ml/min) at 10-MPa backpressure and 15-MPa confining pressure (i.e., the effective stress was constant at 5 MPa). After 20 pore volumes of live-brine injection, the sample was again μCT imaged at the same resolution $(3.43\ \mu m)^3$ in situ.

**Table 2**
*The boundary conditions and associated values and other input parameters.*

| parameter | symbol | value |
|---|---|---|
| brine injection velocity into sandstone | $u_i$ | $10^{-4}$ m/s |
| no-slip boundary condition at four walls | $u_i$ | 0 |
| outlet pressure | p | 0 |
| brine density | ρ | 1042 kg/m$^3$ |
| brine viscosity | μ | $8.899^{-4}$ Pa.s |

The μCT images were then filtered with a 3-D nonlocal means filter (Buades et al., 2005; Onifade et al., 2013) and segmented with a watershed algorithm (Roerdink & Meijster, 2000; Schlüter et al., 2014) for qualitative

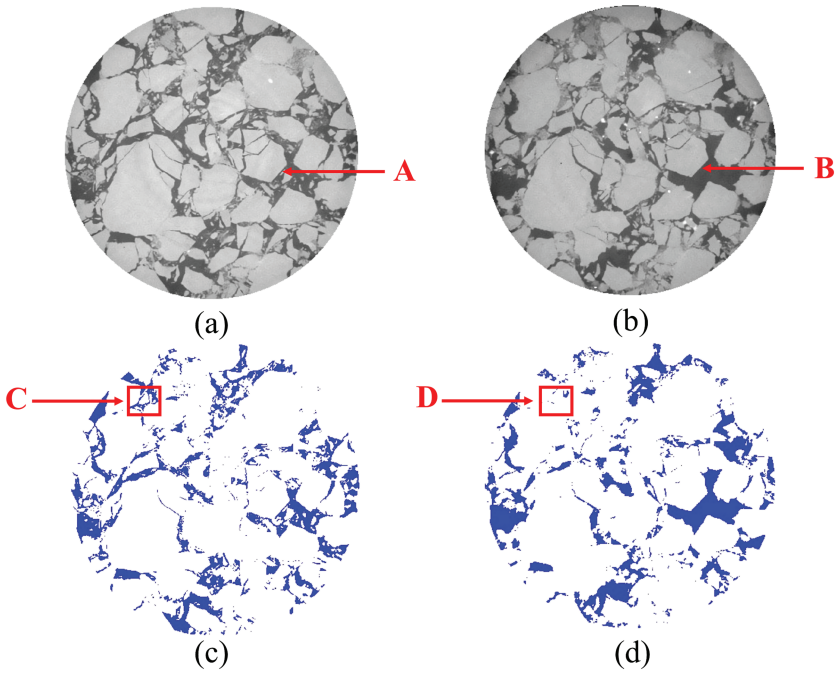


**Figure 6.** 2D slices through the unconsolidated sandstone at in-situ conditions, (a) dry sample; (b) sample after live brine flooding; where the quartz and clay minerals are shown in light colours, whilst, dark colour indicates pores; (c) segmented slice; (d) segmented slice after live brine flooding; pore space is blue, solid is white; arrows A and B indicate fines migration; box C and D show an example where a small pore shrank.

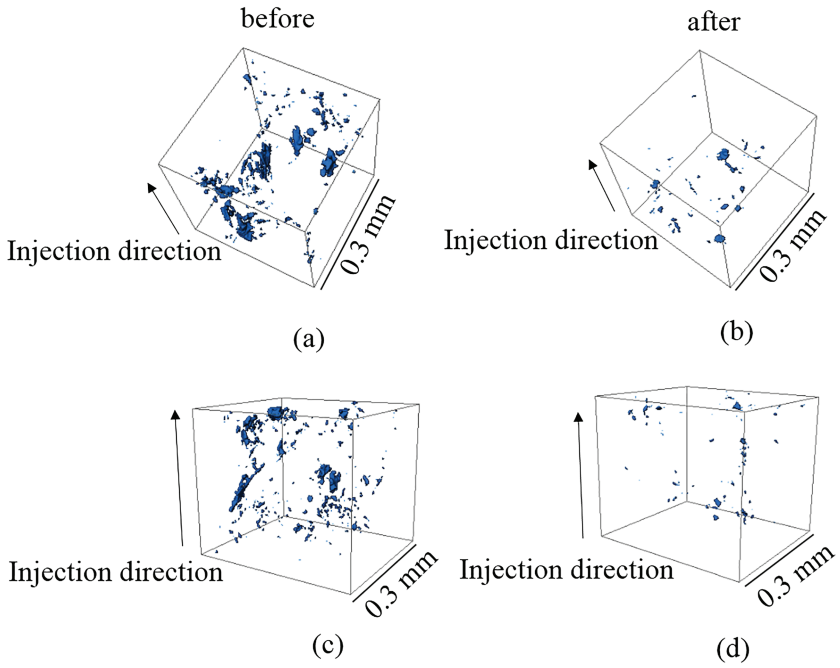


**Figure 7.** 3D visualizations of small pores before and after live brine flooding. (a) and (b) are the same part of sample before and after flooding; where (c) and (d) are the same part of sample before and after flooding. The small pores shrank in size or disappeared completely.

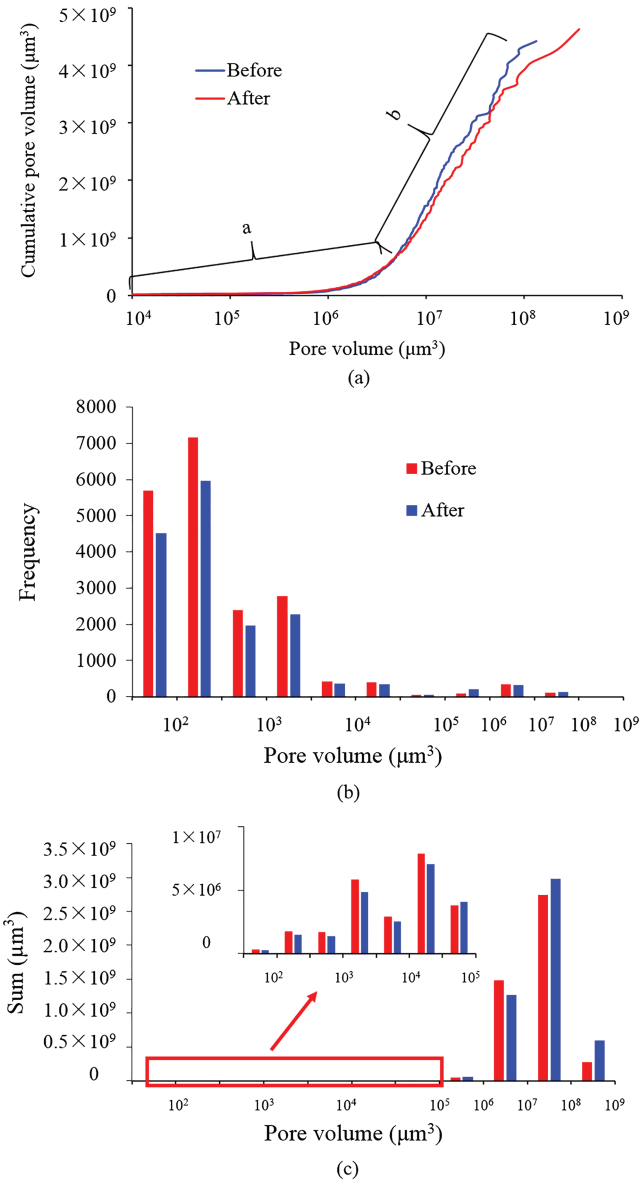


**Figure 8.** Pore size distributions before (blue line) and after (red line) live brine injection.

and quantitative analyses (Figures 4 and 5). The porosity was measured on the microCT images, and the pore size distribution was determined via equivalent sphere analysis (where each pore is considered spherical).

### 2.3. Permeability Analysis

Permeability was examined in detail numerically to determine how precisely it was rendered by the live-brine flooding and which mechanism was responsible for this. Permeability is controlled by the geometry of the connected pore space (Despois & Mortensen, 2005; Doyen, 1988; Lu et al., 2006). Thus all disconnected pores present were truncated in the numerical analysis to reduce mesh size and computational time. Pore spaces were separated from the solid phase and used for triangular surface mesh generation (Chareyre et al., 2012; Genty & Pot, 2014; Talon et al., 2012; Yan et al., 2010). The triangular surface mesh was then imported into a volume mesh generating software, ICEM CFD, to generate the tetrahedral volume mesh for the flow analysis. The quality and ability of the triangular surface mesh to generate the tetrahedral volume mesh was assessed. The tetrahedral element volume was not uniform. The smallest tetrahedral element had the same size as 1 voxel $(3.43\ \mu m)^3$. The volumes of the tetrahedral elements were, however, gradually increased in the wider region to ensure all pore geometry was accurately captured. The grid independent test was performed on a grid size of 1.7M, 2.7M, and 4.4M elements. Each time pressure drop across the sample was estimated (Figure 14c). The difference in pressure drop between 2.7M and 4.4M tetrahedral mesh was 2.8%. To reduce the computational cost and CPU time, 2.7M tetrahedral elements were thus used in the simulation. The sample was $400 \times 400 \times 650$ voxels (1 voxel = $[3.43\ \mu m]^3$). Thus the (digital) sample length in the $z$ direction was measured as 2.232 mm (650 voxels × 3.43 μm). In order to predict brine permeability, we then solved the continuity and Navier-Stokes (Brush & Thomson, 2003) equations.

$$\frac{\partial \rho}{\partial t} + \nabla \cdot (\rho \mathbf{u}) = 0. \tag{1}$$

$$\frac{\partial \rho \mathbf{u}}{\partial t} + \nabla \cdot (\rho \mathbf{u}\mathbf{u}) = -\nabla p + \nabla . \mu \nabla \mathbf{u} + S. \tag{2}$$

The permeability calculations were conducted for the images before and after flooding, so the unsteady state term $\frac{\partial \rho}{\partial t}$ and source term $S$ in equations (1) and (2) were set to 0; $\rho$ is the fluid density, $\mathbf{u}$ is the velocity vector, $p$ is the pressure, and $t$ is time. The computations were performed using a commercially available computational fluid dynamics (CFD) package (ANSYS-CFX; Jaganathan et al., 2008; Truscello et al., 2012), which has a coupled solver (i.e., it simultaneously solves the $u$, $v$, and $w$ momentum of the Navier-Stokes equation) and uses an unstructured mesh based on the element finite volume (FV) method (Droniou, 2014; Rodi, 1997; Wang et al., 2004). FV uses the integral form of the momentum conservation equations as its starting point. The solution domain is subdivided into a finite number of contiguous control volumes (CVs), and the conservation equations are applied to each CV. At the centroid of each CV lies a computational node at which the variable values are calculated. FV can accommodate any grid type, so it is suitable for complex geometries as in the case discussed here. The grid defines only the CV boundaries and it does not need to be related to a coordinate system.

A uniform brine injection velocity inlet boundary condition was specified on one side of the modeled volume, and a pressure boundary condition was prescribed at the outlet (opposite side to the inlet); this reference pressure was set to 0. The pressure at the inlet is therefore equal to the pressure difference between inlet and outlet, that is, the pressure drops across the sample. All the other faces were assumed to be impermeable,

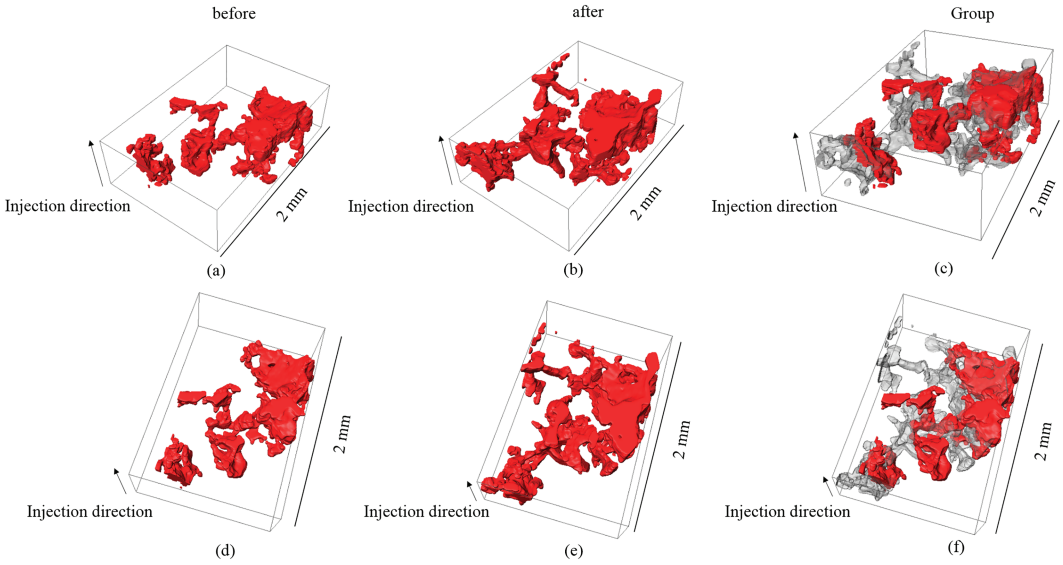


**Figure 9.** 3D visualizations of the enlargement of a large pore in the sample caused by live brine flooding, the grey color in (c) and (f) indicates pore volume added after live brine injection, while the red volume shows the initial pore volume (before flooding).

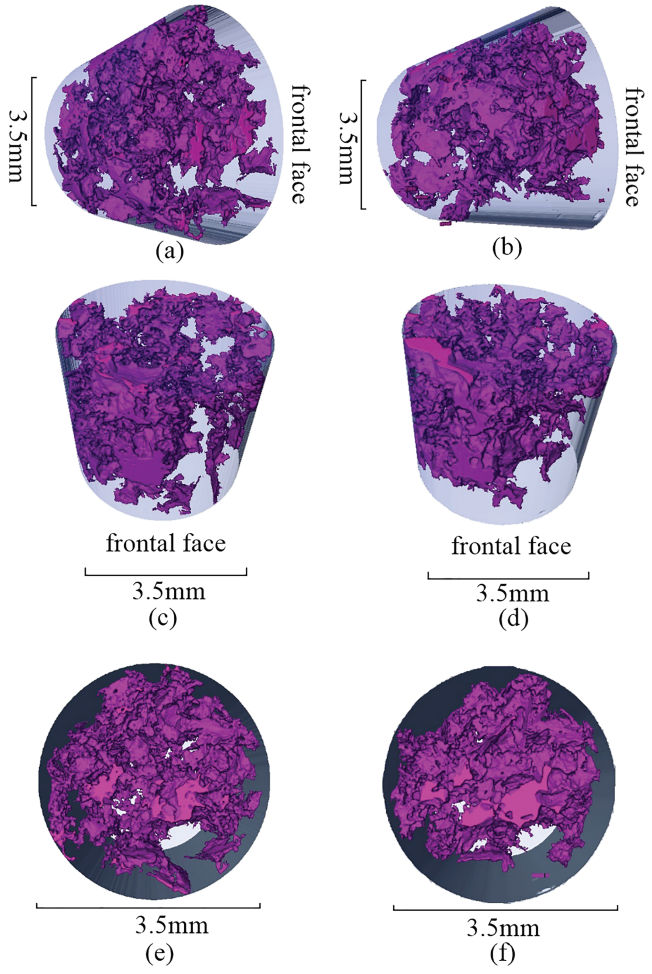


**Figure 10.** 3D visualization of the pore space (only pores larger than $10^7$ $\mu m^3$ are shown); (a, c, e): before; (b, d, e): after live brine injection.

which was computationally achieved by applying no-slip wall boundary conditions. The convergence criterion for all variables was set to $10^{-5}$. Table 2 summarizes the boundary conditions and associated values and other input parameters.

We thus calculated the pressure field and the velocity vector field over all grid elements with CFD. From this information, we computed the pressure gradient across the sample length ($dp/dl$) and used Darcy's law (equation (3); Whitaker, 1986) to calculate the absolute permeability $k$.

$$u = \frac{q}{A} = -\frac{k}{\mu}\frac{dp}{dl}. \tag{3}$$

where $u$ is the area-averaged inlet velocity, $A$ is the cross-sectional area of the sample (here the area at the inlet), $\mu$ is the brine viscosity, and $q$ is the volumetric flow rate.

## 3. Results and Discussion

### 3.1. Changes in the Pore Morphology

Exactly the same volumes were CT imaged before and after flooding. The pore volume fraction (porosity) was measured on the μCT images before and after live-brine injection (compare Figure 6). The pore morphology was extracted from the CT images (Figures 6c and 6d) in the $z$ axis. We did not see large quartz grains reorganized after live-brine injection. However, migration of smaller quartz grains was apparent on the CT images (see Figure 6 [arrows A and B]). Clearly the pore morphology changed after live-brine injection, which led to a slightly increased porosity. Thus, initially, the porosity was 20.8%, which increased to 21.7% after live-brine flooding. Furthermore, pore-size distributions and pore-network structures were extracted via watershed and label analysis algorithms (Barnes et al., 2014; Patras et al., 2001) from the segmented images and analyzed. Label analysis is a tool that permits extraction of statistical and numerical information from CT images, for example, determine the

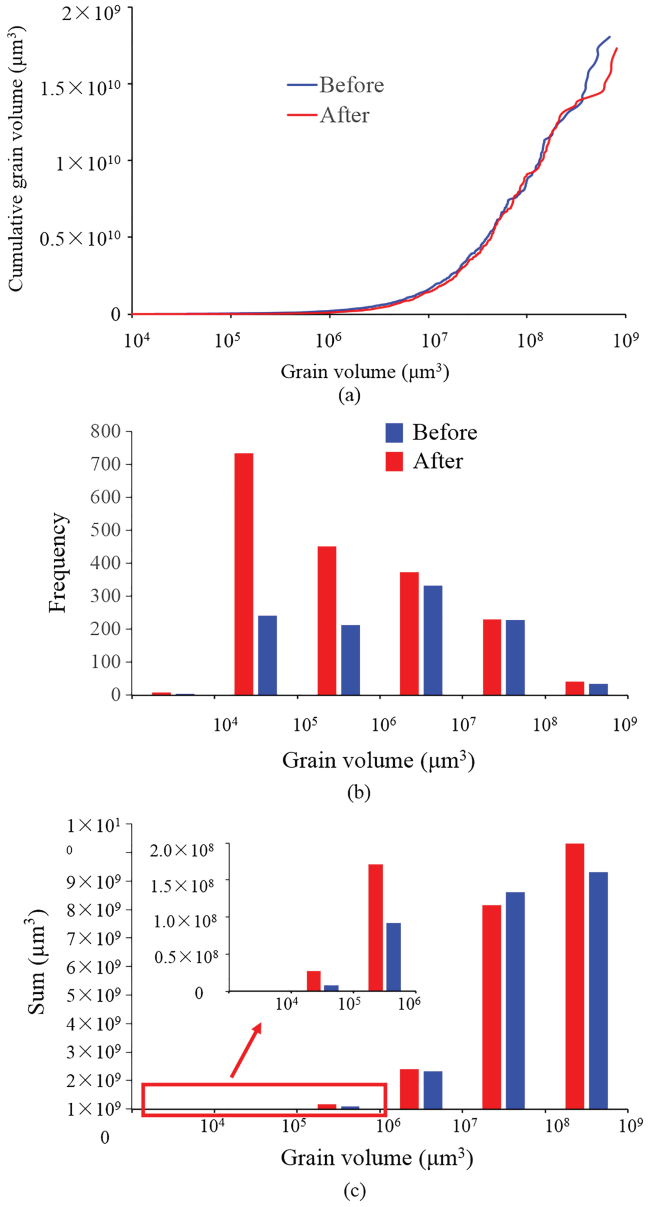


**Figure 11.** Grain size distributions before (blue) and after (red) live brine injection.

equivalent diameter, surface area, or volume for each individual pore (Barnes et al., 2014; Maini & Aggarwal, 2009; Ma et al., 2010). This algorithm performs a connectivity analysis of individual pores within the entire 3-D volume depending on interpretation port, based on voxels size and current units. Surface area uses "intercepts" to take into account the exposed surface of the outer voxels. Equivalent diameter is transferring the irregular shape to an equivalent sphere and then the equivalent spherical diameter in 3-D case is calculated with the volume.

The number of small pores ($<5 \times 10^{-6}$ $\mu m^3$) decreased after live-brine injection (some of them even disappeared; Figure 6), while the number and sum of large pores increased (Figures 7 and 8). This was caused by enlargement of medium-sized pores, as illustrated in Figure 9, where a zoom into the sample (probably 1/15 of the entire sample) is shown.

Note that the large pores, especially those larger than $10^7$ $\mu m^3$, contributed most to the pore space and significantly changed after live-brine flooding (Figure 10). Relate this to the changes in individual grain volumes (Figure 11). Here random changes in grain sizes were observed; some grain sizes increased while others decreased, somewhat independent of their size. However, the sample disintegrates after it was extracted from high-pressure sleeve; we thus cannot conduct a very meaningful scanning electron microscopy analysis on these (disintegrated) samples.

We thus may conclude that pore and grain size changes were maybe caused by mechanical fines migration during live-brine flooding. From the CT images, we can see that the migrated fines include small quartz and clay minerals, and the small quartzes take a big part in all migrated fines. We attribute the slight porosity increase to fines flowing out of the samples as evidenced by the whitish color of the effluent water. Fine particles are usually located on the grain surfaces. The stability of these fine particles is determined by electrostatic, gravitational, drag, adhesion, and lifting forces (Civan, 2007b, 2010; Khilar & Fogler, 1998; Schembre & Kovscek, 2005; Takahashi & Kovscek, 2010; Valdya & Fogler, 1992). While electrostatic, gravitational, and adhesion forces are attractive (i.e., they attach the fine particles to the rock surface), drag and lifting forces may detach the fines particle. There is thus a subtle force balance that determines detachment. Drag forces are again determined by the flow velocity (Zeinijahromi et al., 2012) and pH value (Khilar & Fogler, 1998). pH of the carrier fluid can determine interfacial tension, the wettability of the rock and fine particles, then affect the detached force (Abbasi et al., 2011; Amaefule et al., 1987; Liu & Civan, 1995). Civan (2007) has investigated the critical velocity for different rocks, and the slowest critical velocity (at which detachment occurs due to viscous forces) is 0.01 cm/s while the velocity in this experiment is 0.008 cm/s; we can conclude that the velocity here is sufficiently slow to avoid particle detachment due to drag forces. Note, however, that $CO_2$-saturated brine at high pressure has a significantly reduced pH value (Iglauer et al., 2014; Luquot & Gouze, 2009; Mangane et al., 2013). This effect, we conclude, is the main reason for particle detachment (and thus fines migration).

In addition, Lamy-Chappuis et al. (2014) reported that fines in calcareous sandstone, which detach during flooding will reattach to other grains further downstream, consistent with results reported by Khilar and Fogler (1998) and Sharma and Yortsos (1987) in porous media and Abhishek and Hamouda (2017) in berea sandstone; these fines then reattached to the grains downstream (Civan, 2007a, 2011). This is the main reason for the siginificant changes in pore structure and pore size.

vThe migrated fines actually include small quartz particles and clay minerals together. However, the small quartz particles constitute a large proportion of all migrated fines. From the μCT images, we can see that the

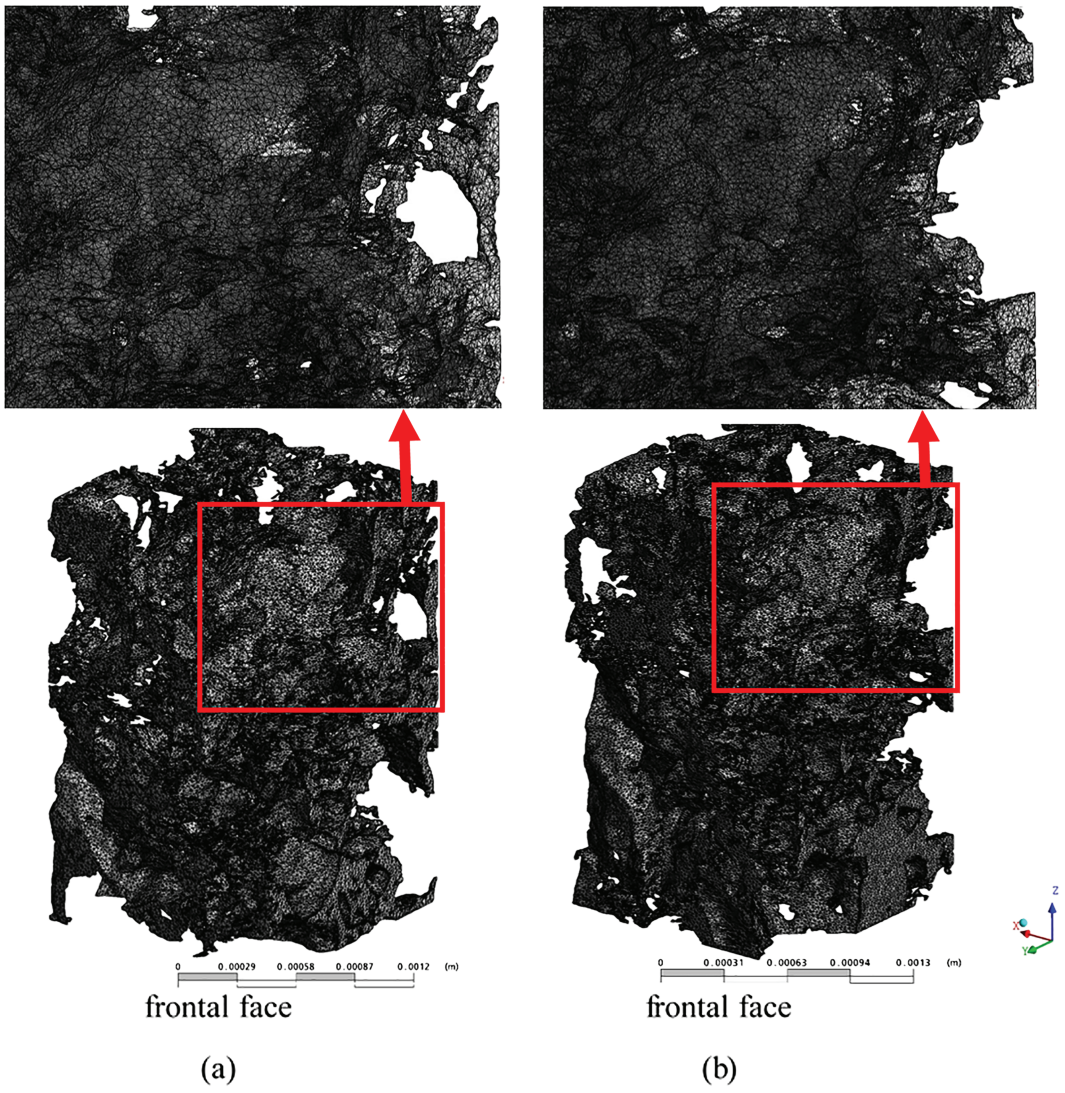


**Figure 12.** Connected pores with mesh (a) before and (b) after live brine flooding.

fines particles are mechanically trapped in the narrow pore throats, which is clearly a physical deposition. Process wise, we have segmented three phases: porosity, quartz, and clay. However, the big quartz grains from the major quartz phase (>90%), we thus cannot see small quartz grains clearly on the associated 3-D quartz visualizations. In conclusion, it is better to assess the 3-D porosity to analyze the impact of fines migration.

### 3.2. Permeability Evolution

Brine permeability was calculated in the $z$ direction parallel to the bedding plane. Figures 12a and 12b show the connected pores with mesh used for this flow analysis (before and after live-brine flooding). The live brine entered into the sample from the bottom and exited from the top. The pressure fields during flow (the Darcy velocity for both pore systems at the inlet was $1.0 \times 10^{-4}$ m/s, which represented laminar Darcy flow) are shown in Figure 13, and the area-averaged pressure at the inlet (bottom red zone) was ≈10 and ≈20 Pa, respectively, before and after live-brine flooding. The pressure gradually dropped from bottom to top in the sample before core flooding (Figure 13a; from 10 to 0 Pa). However, the pressure difference was higher in the sample after core flooding; moreover, there was no gentle pressure drop from bottom to the middle of the sample anymore, instead a sudden pressure drop from 20 to 10 Pa (red boxes in Figure 13) and finally 0 Pa at the top appeared, which is also shown in Figure 13c. Hence, the sample became less permeable

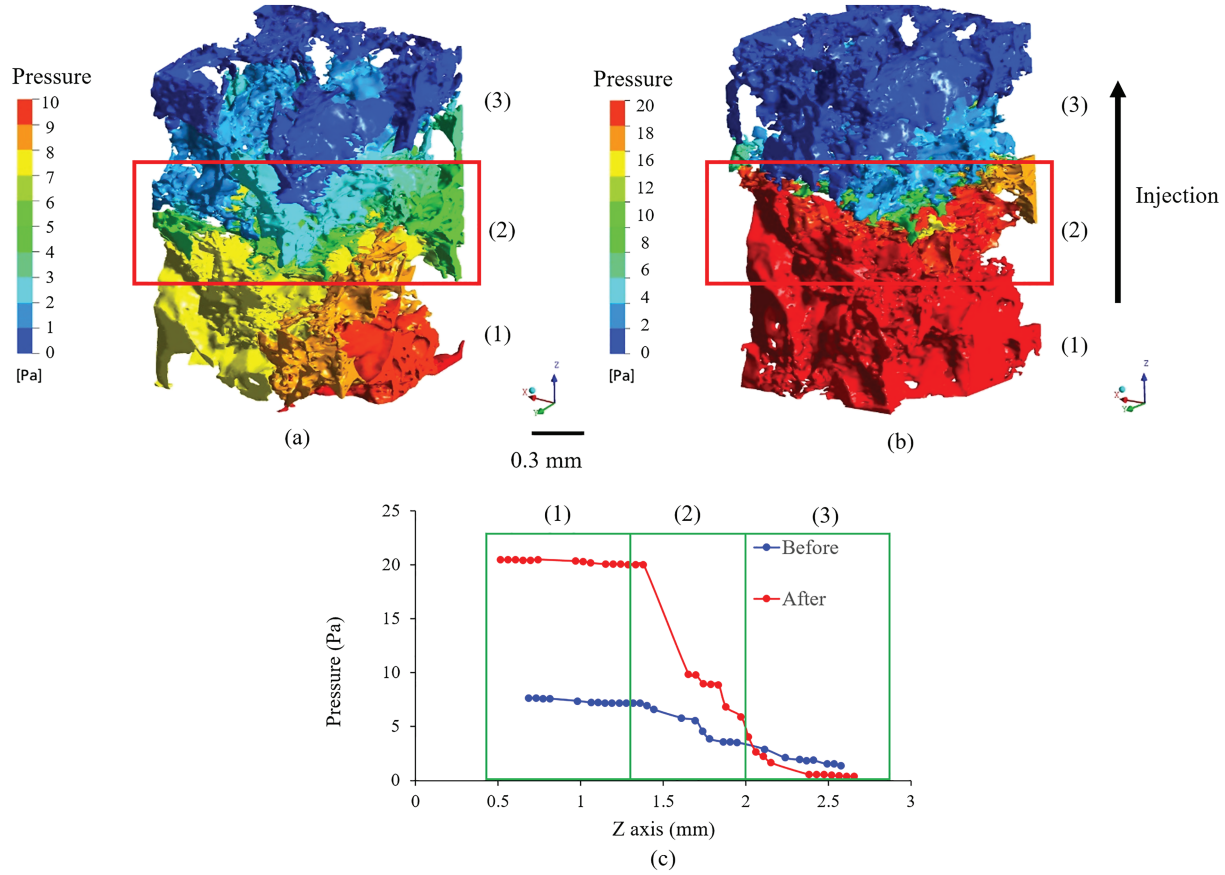


**Figure 13.** Pressure field during flow for the unconsolidated sandstone sample; (a) before, (b) after live brine flooding, (c) pressure plotted versus core length; the red box shows the drastic reduction in pressure in the middle of the sample after live brine flooding.

after live-brine injection. We also subsampled three subdomains (Figure 12) namely, the frontal part (1), the interior part (the barrier; 2), and the basal part (3). The permeability increased significantly in the frontal part (1) from 21.55 D to 57.24 D while in the middle and end part, it dramatically dropped from 13.55 D to 4.07 D in the middle and from 23.39 D to 13.49 D (Table 3). This analysis verifies that fines migrated downstream and blocked mainly the interior and also the basal part. Fines transported by the live brine reattached in the downstream part of the sample as indicated by the pressure analysis and examination of the pore-space morphology. Specifically, these fines aggregated in pore throats and blocked some flow paths; thus, the frontal part of the plug was left more permeable. These changes in pore morphology thus changed the velocity field (Civan, 2010; Civan & Knapp, 1987; Tang & Morrow, 1999). Clearly, the velocity increased significantly in the middle part of the sample after live-brine flooding, especially in the red box (Figure 14). An analysis of the cross section of the dataset in the *x-y* plane (Figure 16 c [Figure 14 now]; $z = 0.00174858$ m, middle of red box region) was shown as following. The analysis revealed that the porosity in this plane was reduced by 13% after live-brine injection. The pore size and distribution were totally changed due to fines blocking the pores and throats, leading to higher velocities in this plane (to maintain a constant flow rate). Thus, the reduction in permeability is a combined effect of both porosity and pore size reduction.

**Table 3**
*The permeability before and after core flooding.*

| Permeability (D) | (1) | (2) | (3) |
|---|---|---|---|
| Before | 21.55 | 13.55 | 23.39 |
| After | 57.24 | 4.07 | 13.49 |

Substituting these values into Darcy's equation, a brine permeability of 18.34 D was predicted (in the *z* direction) before core flooding, which dramatically decreased to 9.17 D after live-brine flooding, even though the porosity only increased slightly (from 20.8% to 21.7%, see above). It thus can be deduced that fines migration is the dominant mechanism influencing permeability in unconsolidated sandstone and that fines migration clearly decreased permeability, which is detrimental for $CO_2$ injection.

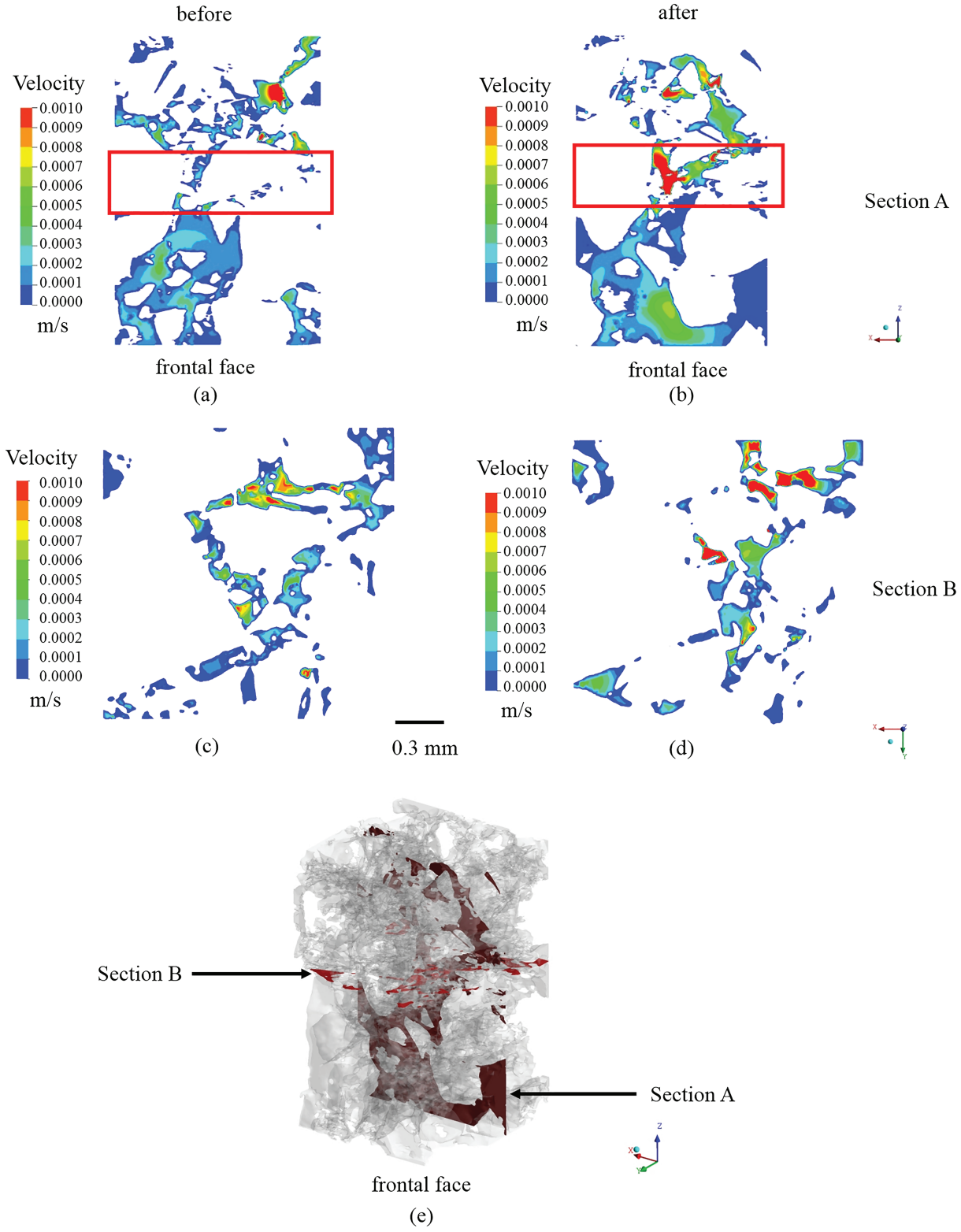


**Figure 14.** Velocity contours shown on two planes sliced parallel and normal through the sample. (a) Before and (b) after core flooding of section A, (c) before and (d) after core flooding of cross section B, (e) Red planes indicate where the illustrated planes were sliced.

## 4. Conclusions

It has previously been observed for consolidated sandstone, where Mg-calcite dissolved, that a higher permeability resulted (Gray et al., 2018; Luquot & Gouze, 2009). In order to clarify how the pore morphology in unconsolidated sandstone changes and how precisely the permeability is affected, we investigated how the petrophysical properties of an unconsolidated sandstone are rendered by $CO_2$-saturated (live) brine injection via in situ X-ray μCT, simulating true storage conditions. We also examined the permeability evolution in the sample numerically via CFD to identify the underlying mechanisms responsible for the observed permeability reduction.

Indeed, the pore morphology was changed by the live brine, and large pores were enlarged while small pores shrank or even disappeared. This was due to fines that were initially located on the surface of the quartz grains or filled in the pores, which were mobilized but reattached to the other grains further downstream, particularly in pore throats. We conclude that the pore structure of the examined unconsolidated sandstone can be significantly changed after live-brine injection, although the porosity is only slightly affected.

As a consequence, the permeability of the examined core decreased during live-brine flooding. The numerical analysis showed that this is due to pore throat blockage in the middle and basal parts of the sample, again indicating fines migration as the responsible mechanism It maybe thus be expected from this type of formation that $CO_2$ injectivity drastically decreases during $CO_2$ injection in unconsolidated sandstone reservoirs, which will limit storage capacities.

**Acknowledgments**
This work was jointly funded by National Natural Science Foundation of China (41902145), and National and Local Joint Engineering Research Center for Carbon Capture Utilization and Sequestration at Northwest University in China and Young Talent fund of University Association for Science and Technology in Shaanxi, China (20180701). The measurements were performed using the micro CT system of the National Geosequestration Laboratory (NGL) of Australia. Funding for the facilities was provided by the Australian Federal Government. This work was also supported by the Pawsey Supercomputing Centre, who provided the Avizo 9.2 image processing software and workstation, with funding from the Australian Government and the Government of Western Australia. Experimental test data for all samples can be obtained at https://github.com/AMELIAYUNWU/unconsolidated-sandstone.

## References

Abbasi S, Shahrabadi A, Golghanddashti H (2011), Experimental Investigation of clay minerals' effects on the permeability//SPE European Formation Damage Conference. Society of Petroleum Engineers.

Abhishek, R., & Hamouda, A. A. (2017). Effect of various silica nanofluids: Reduction of fines migrations and surface modification of berea sandstone. *Applied Sciences*, *7*(12), 1216. https://doi.org/10.3390/app7121216

Acquafredda, P., & Paglionico, A. (2004). SEM-EDS microanalysis of microphenocrysts of Mediterranean obsidians: A preliminary approach to source discrimination. *European Journal of Mineralogy*, *16*(3), 419–429. https://doi.org/10.1127/0935-1221/2004/0016-0419

Al-Khdheeawi, E. A., Vialle, S., Barifcani, A., Sarmadivaleh, M., & Iglauer, S. (2017). Impact of reservoir wettability and heterogeneity on $CO_2$-plume migration and trapping capacity. *International Journal of Greenhouse Gas Control*, *58*, 142–158. https://doi.org/10.1016/j.ijggc.2017.01.012

Al-Khdheeawi, E. A., Vialle, S., Barifcani, A., Sarmadivaleh, M., & Iglauer, S. (2018). Effect of wettability heterogeneity and reservoir temperature on $CO_2$ storage efficiency in deep saline aquifers. *International Journal of Greenhouse Gas Control*, *68*, 216–229. https://doi.org/10.1016/j.ijggc.2017.11.016

Alvarez, A. C., Hime, G., Dan, M., & Bedrikovetsky, P. G. (2006). A fast inverse solver for the filtration function for flow of water with particles in porous media. *Inverse Problems*, *22*(1), 69–88. https://doi.org/10.1088/0266-5611/22/1/005

Al-Yaseri, A., Lebedev, M., Barifcani, A., & Iglauer, S. (2016). Impact of fines and rock wettability on reservoir formation damage. *Geophysical Prospecting*, *64*(4), 860–874. https://doi.org/10.1111/1365-2478.12379

Al-Yaseri, A. Z., Lebedev, M., Vogt, S. J., Johns, M. L., Barifcani, A., & Iglauer, S. (2015). Pore-scale analysis of formation damage in Bentheimer sandstone with in-situ NMR and micro-computed tomography experiments. *Journal of Petroleum Science & Engineering*, *129*, 48–57. https://doi.org/10.1016/j.petrol.2015.01.018

Al-Yaseri, A. Z., Zhang, Y., Ghasemiziarani, M., Sarmadivaleh, M., Lebedev, M., Roshan, H., et al. (2017). Permeability evolution in sandstone due to $CO_2$ injection. *Energy & Fuels*, *31*(11), 12,390–12,398. https://doi.org/10.1021/acs.energyfuels.7b01701

Amaefule J O, Ajufo A, Peterson E (1987). [Society of Petroleum Engineers SPE Production Operations Symposium - Oklahoma City, Oklahoma] SPE Production Operations Symposium - Understanding formation damage processes: An essential ingredient for improved measurement and interpretation of relative permeability data. SPE Production Operations Symposium.

Bachu, S. (2015). Review of $CO_2$ storage efficiency in deep saline aquifers. *International Journal of Greenhouse Gas Control*, *40*, 188–202. https://doi.org/10.1016/j.ijggc.2015.01.007

Baker, J. C., Uwins, P. J. R., & Mackinnon, I. D. R. (1993). ESEM study of authigenic chlorite acid sensitivity in sandstone reservoirs. *Journal of Petroleum Science & Engineering*, *8*(4), 269–277. https://doi.org/10.1016/0920-4105(93)90004-X

Barnes, R., Lehman, C., & Mulla, D. (2014). Priority-flood: An optimal depression-filling and watershed-labeling algorithm for digital elevation models. *Computers & Geosciences*, *62*(1), 117–127. https://doi.org/10.1016/j.cageo.2013.04.024

Bedrikovetsky, P., Siqueira, F. D., Furtado, C. A., & Souza, A. L. S. D. (2012). Particle detachment under velocity alternation during suspension transport in porous media. *Transport in Porous Media*, *91*(1), 173–197. https://doi.org/10.1007/s11242-011-9839-1

Bertos, M., Fernández, S. J., Simons, R., Hills, C. D., & Carey, P. J. (2004). A review of accelerated carbonation technology in the treatment of cement-based materials and sequestration of $CO_2$. *Journal of Hazardous Materials*, *112*(3), 193–205. https://doi.org/10.1016/j.jhazmat.2004.04.019

Brush, D. J., & Thomson, N. R. (2003). Fluid flow in synthetic rough-walled fractures: Navier-Stokes, Stokes, and local cubic law simulations. *Water Resources Research*, *39*(4), 1085. https://doi.org/10.1029/2002wr001346

Buades, A., B. Coll, and J. M. Morel (2005), A non-local algorithm for image denoising, paper presented at computer vision and pattern recognition, 2005. CVPR 2005. IEEE Computer Society Conference on Computer Vision & Pattern Recognition.

Chareyre, B., Catalano, E., & Barthélemy, E. (2012). Pore-scale modeling of viscous flow and induced forces in dense sphere packings. *Transport in Porous Media*, *94*(2), 595–615. https://doi.org/10.1007/s11242-012-0057-2

Chen, X., Gao, S., Kianinejad, A., & Dicarlo, D. A. (2017). Steady-state supercritical co$_2$ and brine relative permeability in berea sandstone at different temperature and pressure conditions. *Water Resources Research*, *53*, 6312–6321. https://doi.org/10.1002/2017WR020810

Civan, F. (2007a). Reservoir formation damage *(Second Edition)*.

Civan, F. (2007b). Temperature effect on power for particle detachment from pore wall described by an arrhenius-type equation. *Transport in Porous Media*, *67*(2), 329–334. https://doi.org/10.1007/s11242-006-9005-3

Civan, F. (2010). Non-isothermal permeability impairment by fines migration and deposition in porous media including dispersive transport. *Transport in Porous Media*, *85*(1), 233–258. https://doi.org/10.1007/s11242-010-9557-0

Civan, F. (2011). *Porous media transport phenomena*. Wiley. https://doi.org/10.1002/9781118086810

Civan, F., and R. M. Knapp (1987), Effect of clay swelling and fines migration on formation permeability, *SPE Production Operations Symposium*.

Despois, J. F., & Mortensen, A. (2005). Permeability of open-pore microcellular materials. *Acta Materialia*, *53*(5), 1381–1388. https://doi.org/10.1016/j.actamat.2004.11.031

Ding, W., Zhu, D., Cai, J., Gong, M., & Chen, F. (2013). Analysis of the developmental characteristics and major regulating factors of fractures in marine-continental transitional shale-gas reservoirs: A case study of the Carboniferous-Permian strata in the southeastern Ordos Basin, central China. *Marine & Petroleum Geology*, *45*(4), 121–133. https://doi.org/10.1016/j.marpetgeo.2013.04.022

Doyen, P. M. (1988). Permeability, conductivity, and pore geometry of sandstone. *Journal of Geophysical Research Solid Earth*, *93*(B7), 7729–7740. https://doi.org/10.1029/JB093iB07p07729

Droniou, J. (2014). Finite volume schemes for diffusion equations: Introduction to and review of modern methods. *Mathematical Models & Methods in Applied Sciences*, *24*(08), 1575–1619. https://doi.org/10.1142/S0218202514400041

Duan, Y., Wang, C. Y., Zheng, C. Y., Wu, B. X., & Zheng, G. D. (2008). Geochemical study of crude oils from the Xifeng oilfield of the Ordos Basin, China. *Journal of Asian Earth Sciences*, *31*(4-6), 341–356. https://doi.org/10.1016/j.jseaes.2007.05.003

El-Maghraby, R. M., Pentland, C. H., & Iglauer, S. (2012). A fast method to equilibrate carbon dioxide with brine at high pressure and elevated temperature including solubility measurements. *Journal of Supercritical Fluids*, *62*(none), 55–59. https://doi.org/10.1016/j.supflu.2011.11.002

Genty, A., & Pot, V. (2014). Numerical calculation of effective diffusion in unsaturated porous media by the TRT Lattice Boltzmann method. *Transport in Porous Media*, *105*(2), 391–410. https://doi.org/10.1007/s11242-014-0374-8

Gray, F., Anabaraonye, B., Shah, S., Boek, E., & Crawshaw, J. (2018). Chemical mechanisms of dissolution of calcite by HCl in porous media: Simulations and experiment. *Advances in Water Resources*, *121*, 369–387. https://doi.org/10.1016/j.advwatres.2018.09.007

Gruesbeck, C., & Collins, R. E. (1982). Entrainment and deposition of fine particles in porous media. *Soc. Pet. Eng. AIME, Pap.; (United States)*, *22*(6), 847–856. https://doi.org/10.2118/8430-pa

Han, W. S., Lee, S. Y., Lu, C., & Mcpherson, B. J. (2010). Effects of permeability on $CO_2$ trapping mechanisms and buoyancy-driven $CO_2$ migration in saline formations. *Water Resources Research*, *46*, W07510. https://doi.org/10.1029/2009wr007850

Hangx, S., Bakker, E., Bertier, P., Nover, G., & Busch, A. (2015). Chemical–mechanical coupling observed for depleted oil reservoirs subjected to long-term $CO_2$-exposure-A case study of the Werkendam natural $CO_2$ analogue field. *Earth & Planetary Science Letters*, *428*, 230–242. https://doi.org/10.1016/j.epsl.2015.07.044

Iglauer, S., Al-Yaseri, A. Z., Rezaee, R., & Lebedev, M. (2016). $CO_2$-wettability of caprocks: Implications for structural storage capacity and containment security. *Geophysical Research Letters*, *42*, 9279–9284. https://doi.org/10.1002/2015gl065787

Iglauer, S., & Lebedev, M. (2017). High pressure-elevated temperature X-ray micro-computed tomography for subsurface applications. *Advances in Colloid & Interface Science*, *256*, 393–410.

Iglauer, S., Sarmadivaleh, M., Al-Yaseri, A., & Lebedev, M. (2014). Permeability evolution in sandstone due to injection of $CO_2$-saturated brine or supercritical $CO_2$ at reservoir conditions. *Energy Procedia*, *63*, 3051–3059. https://doi.org/10.1016/j.egypro.2014.11.328

Jaganathan, S., Tafreshi, H. V., & Pourdeyhimi, B. (2008). A realistic approach for modeling permeability of fibrous media: 3-D imaging coupled with CFD simulation. *Chemical Engineering Science*, *63*(1), 244–252. https://doi.org/10.1016/j.ces.2007.09.020

Kampman, N., Bickle, M., Wigley, M., & Dubacq, B. (2014). Fluid flow and $CO_2$-fluid-mineral interactions during $CO_2$-storage in sedimentary basins. *Chemical Geology*, *369*(4), 22–50. https://doi.org/10.1016/j.chemgeo.2013.11.012

Ketzer, J. M., Iglesias, R., Einloft, S., Dullius, J., Ligabue, R., & Lima, V. D. (2009). Water-rock-CO interactions in saline aquifers aimed for carbon dioxide storage: Experimental and numerical modeling studies of the Rio Bonito Formation (Permian), southern Brazil. *Applied Geochemistry*, *24*(5), 760–767. https://doi.org/10.1016/j.apgeochem.2009.01.001

Khilar, K. C., & Fogler, H. S. (1998). *Migrations of Fines in Porous Media*. Netherlands: Springer. https://doi.org/10.1007/978-94-015-9074-7

Lai, J., Wang, G., Ran, Y., Zhou, Z., & Cui, Y. (2016). Impact of diagenesis on the reservoir quality of tight oil sandstones: The case of Upper Triassic Yanchang Formation Chang 7 oil layers in Ordos Basin, China. *Journal of Petroleum Science & Engineering*, *145*, 54–65. https://doi.org/10.1016/j.petrol.2016.03.009

Lamy-Chappuis, B., Angus, D., Fisher, Q., Grattoni, C., & Yardley, B. W. D. (2014). Rapid porosity and permeability changes of calcareous sandstone due to $CO_2$ enriched brine injection. *Geophysical Research Letters*, *41*, 399–406. https://doi.org/10.1002/2013GL058534

Lebedev, M., Zhang, Y., Mikhaltsevitch, V., Inglauer, S., & Rahman, T. (2017). Residual trapping of supercritical $CO_2$: Direct pore-scale observation using a low cost pressure cell for micro computer tomography. *Energy Procedia*, *114*, 4967–4974. https://doi.org/10.1016/j.egypro.2017.03.1639

Lebedev, M., Zhang, Y., Sarmadivaleh, M., Barifcani, A., Al-Khdheeawi, E., Iglauer, S., et al. (2017). Carbon geosequestration in limestone: Pore-scale dissolution and geomechanical weakening. *International Journal of Greenhouse Gas Control*, *66*, 106–119. https://doi.org/10.1016/j.ijggc.2017.09.016

Lemon, P., Zeinijahromi, A., Bedrikovetsky, P., & Shahin, I. (2011). Effects of injected-water salinity on waterflood sweep efficiency through induced fines migration. *Journal of Canadian Petroleum Technology*, *50*(9/10), 82–94. https://doi.org/10.2118/140141-PA

Liu, M., Shabaninejad, M., & Mostaghimi, P. (2018). Predictions of permeability, surface area and average dissolution rate during reactive transport in multi-mineral rocks. *Journal of Petroleum Science & Engineering*, *170*, 130–138. https://doi.org/10.1016/j.petrol.2018.06.010

Liu X, Civan F (1995). Formation damage by fines migration including effects of filter cake, pore compressibility, and non-darcy flow-A modeling approach to scaling from core to field//SPE International Symposium on Oilfield Chemistry. Society of Petroleum Engineers.

Lu, S., Landis, E. N., & Keane, D. T. (2006). X-ray microtomographic studies of pore structure and permeability in Portland cement concrete. *Materials & Structures*, *39*(6), 611–620.

Luhmann, A. J., Tutolo, B. M., Bagley, B. C., Mildner, D. F. R., Seyfried, W. E., & Saar, M. O. (2017). Permeability, porosity, and mineral surface area changes in basalt cores induced by reactive transport of $CO_2$-rich brine. *Water Resources Research*, *53*, 1908–1927. https://doi.org/10.1002/2016WR019216

Luquot, L., & Gouze, P. (2009). Experimental determination of porosity and permeability changes induced by injection of $CO_2$ into carbonate rocks. *Chemical Geology*, *265*(1-2), 148–159. https://doi.org/10.1016/j.chemgeo.2009.03.028

Ma, Z., Tavares, J. M. R. S., & Jorge, R. N. (2010). A review of algorithms for medical image segmentation and their applications to the female pelvic cavity. *Computer Methods in Biomechanics and Biomedical Engineering*, *13*(2), 235–246. https://doi.org/10.1080/10255840903131878

Maini, R., & Aggarwal, H. (2009). Study and comparison of various image edge detection techniques. *International Journal of Image Processing (IJIP)*, *3*(1), 1–11.

Mangane, P. O., Gouze, P., & Luquot, L. (2013). Permeability impairment of a limestone reservoir triggered by heterogeneous dissolution and particles migration during $CO_2$-rich injection. *Geophysical Research Letters*, *40*, 4614–4619. https://doi.org/10.1002/grl.50595

March, R., Doster, F., & Geiger, S. (2018). Assessment of $CO_2$ storage potential in naturally fractured reservoirs with dual-porosity models. *Water Resources Research*, *54*(3), 1650–1668. https://doi.org/10.1002/2017WR022159

Martinez, M. J., & Hesse, M. A. (2016). Two-phase convective $CO_2$ dissolution in saline aquifers. *Water Resources Research*, *52*, 585–599. https://doi.org/10.1002/2015WR017085

Nordbotten, J. M., Celia, M. A., & Bachu, S. (2005). Injection and storage of CO in deep saline aquifers: Analytical solution for CO plume evolution during injection. *Transport in Porous Media*, *58*(3), 339–360. https://doi.org/10.1007/s11242-004-0670-9

Onifade, I., Jelagin, D., Guarin, A., Birgisson, B., & Kringos, N. (2013). *Asphalt internal structure characterization with X-ray computed tomography and digital image processing*, (pp. 139–158). Springer Netherlands.

Patras, I., Hendriks, E. A., & Lagendijk, R. L. (2001). Video segmentation by MAP labeling of watershed segments. *IEEE Trans.pattern Anal. machine Intell*, *23*(3), 326–332. https://doi.org/10.1109/34.910886

Pentland, C. H., El-Maghraby, R., Iglauer, S., & Blunt, M. J. (2011). Measurements of the capillary trapping of supercritical carbon dioxide in Berea Sandstone. *Geophysical Research Letters*, *38*, L06401. https://doi.org/10.1029/2011gl046683

Pini, R., Krevor, S. C. M., & Benson, S. M. (2012). Capillary pressure and heterogeneity for the $CO_2$/water system in sandstone rocks at reservoir conditions. *Advances in Water Resources*, *38*(2), 48–59. https://doi.org/10.1016/j.advwatres.2011.12.007

Qajar, J., N. Francois, and C. Arns (2012), Micro-tomographic Characterization of dissolution-induced local porosity changes including fines migration in carbonate rock, paper presented at SPE EOR Conference at Oil and Gas West Asia.

Reynolds, C., Blunt, M., & Krevor, S. (2014). Impact of reservoir conditions on $co_2$-brine relative permeability in sandstones. *Energy Procedia*, *63*, 5577–5585. https://doi.org/10.1016/j.egypro.2014.11.591

Rodi, W. (1997). Status of large eddy simulation: Results of a workshop. *Asme Journal of Fluids Engineering*, *119*(2), 248–262. https://doi.org/10.1115/1.2819128

Roerdink, J. B. T. M., & Meijster, A. (2000). The watershed transform: Definitions, algorithms and parallelization strategies. *Fundamenta Informaticae*, *41*(1,2), 187–228.

Schembre, J. M., & Kovscek, A. R. (2005). Mechanism of formation damage at elevated temperature. *Journal of Energy Resources Technology*, *127*(3), 171–180. https://doi.org/10.1115/1.1924398

Schlüter, S., Sheppard, A., Brown, K., & Wildenschild, D. (2014). Image processing of multiphase images obtained via X-ray microtomography: A review. *Water Resources Research*, *50*, 3615–3639. https://doi.org/10.1002/2014WR015256

Sharma, M. M., & Yortsos, Y. C. (1987). Fines migration in porous media. *Aiche Journal*, *33*(10), 1654–1662. https://doi.org/10.1002/aic.690331009

Shi, J. Q., Xue, Z., & Durucan, S. (2011). Supercritical $CO_f$ core flooding and imbibition in Tako sandstone-influence of sub-core scale heterogeneity. *International Journal of Greenhouse Gas Control*, *5*(1), 75–87. https://doi.org/10.1016/j.ijggc.2010.07.003

Sigfusson, B., Gislason, S. R., Matter, J. M., Stute, M., Gunnlaugsson, E., Gunnarsson, I., et al. (2015). Solving the carbon-dioxide buoyancy challenge: The design and field testing of a dissolved $CO_2$ injection system. *International Journal of Greenhouse Gas Control*, *37*, 213–219. https://doi.org/10.1016/j.ijggc.2015.02.022

Smith, M. M., Sholokhova, Y., Hao, Y., & Carroll, S. A. (2013). $CO_2$-induced dissolution of low permeability carbonates. Part I: Characterization and experiments. *Advances in Water Resources*, *62*(12), 370–387. https://doi.org/10.1016/j.advwatres.2013.09.008

Takahashi, S., & Kovscek, A. R. (2010). Wettability estimation of low-permeability, siliceous shale using surface forces. *Journal of Petroleum Science and Engineering*, *75*(1-2), 33–43. https://doi.org/10.1016/j.petrol.2010.10.008

Talon, L., Bauer, D., Gland, N., Youssef, S., Auradou, H., & Ginzburg, I. (2012). Assessment of the two relaxation time Lattice-Boltzmann scheme to simulate Stokes flow in porous media. *Water Resources Research*, *48*, W04526. https://doi.org/10.1029/2011wr011385

Tang, G. Q., & Morrow, N. R. (1999). Influence of brine composition and fines migration on crude oil/brine/rock interactions and oil recovery. *Journal of Petroleum Science & Engineering*, *24*(2-4), 99–111. https://doi.org/10.1016/S0920-4105(99)00034-0

Truscello, S., Kerckhofs, G., Bael, S. V., Pyka, G., Schrooten, J., & Oosterwyck, H. V. (2012). Prediction of permeability of regular scaffolds for skeletal tissue engineering: A combined computational and experimental study. *Acta Biomaterialia*, *8*(4), 1648–1658. https://doi.org/10.1016/j.actbio.2011.12.021

Valdya, R. N., & Fogler, H. S. (1992). Fines migration and formation damage: Influence of pH and ion exchange. *SPE Production Engineering*, *7*(04), 325–330. https://doi.org/10.2118/19413-PA

Wang, Z. J., Zhang, L., & Liu, Y. (2004). Spectral (finite) volume method for conservation laws on unstructured grids IV: Extension to two-dimensional systems. *Journal of Computational Physics*, *194*(2), 716–741. https://doi.org/10.1016/j.jcp.2003.09.012

Whitaker, S. (1986). Flow in porous media I: A theoretical derivation of Darcy's law. *Transport in Porous Media*, *1*(1), 3–25. https://doi.org/10.1007/BF01036523

Wigand, M., Carey, J. W., Schütt, H., Spangenberg, E., & Erzinger, J. (2008). Geochemical effects of CO sequestration in sandstones under simulated in situ conditions of deep saline aquifers. *Applied Geochemistry*, *23*(9), 2735–2745. https://doi.org/10.1016/j.apgeochem.2008.06.006

Wigley, M., Kampman, N., Dubacq, B., & Bickle, M. (2017). Fluid-mineral reactions and trace metal mobilization in an exhumed natural $CO_2$ reservoir, Green River, Utah. *Geology*, *40*(6), 555–558.

Yan, Z., Geiger, S., Sorbie, K., & Förster, M. (2010). Efficient flow and transport simulations in reconstructed 3D pore geometries. *Advances in Water Resources*, *33*(12), 1508–1516.

Yang, Y., Li, W., & Ma, L. (2005). Tectonic and stratigraphic controls of hydrocarbon systems in the Ordos Basin: A multicycle cratonic basin in Central China. *AAPG Bulletin*, *89*(2), 255–269. https://doi.org/10.1306/10070404027

Yasuda, E. Y., Santos, R. G. D., & Vidal Trevisan, O. (2013). Kinetics of carbonate dissolution and its effects on the porosity and permeability of consolidated porous media. *Journal of Petroleum Science and Engineering*, *112*, 284–289. https://doi.org/10.1016/j.petrol.2013.11.015

Zeinijahromi, A., Vaz, A., & Bedrikovetsky, P. (2012). Well impairment by fines migration in gas fields. *Journal of Petroleum Science & Engineering*, *88-89*, 125–135. https://doi.org/10.1016/j.petrol.2012.02.002

Zhang, W. Z., Hua, Y., Jian-Feng, L. I., & Jun, M. A. (2006). Leading effect of high-class source rock of Chang 7 in Ordos Basin on enrichment of low permeability oil-gas accumulation-Hydrocarbon generation and expulsion mechanism. *Petroleum Exploration & Development*, *33*(3), 289–293.

Zhang, Y., Lebedev, M., Sarmadivaleh, M., Barifcani, A., & Iglauer, S. (2016). Swelling-induced changes in coal microstructure due to supercritical $CO_2$ injection. *Geophysical Research Letters*, *43*, 9077–9083. https://doi.org/10.1002/2016GL070654

Zhu, H., Liu, K., Yang, X., & Liu, Q. (2013). Sedimentary controls on the sequence stratigraphic architecture in intra-cratonic basins: An example from the lower Permian Shanxi formation, Ordos Basin, northern China. *Marine & Petroleum Geology*, *45*, 42–54. https://doi.org/10.1016/j.marpetgeo.2013.04.017